Catalysis Science & Technology

PAPER

View Article Online
View Journal | View Issue

Cite this: *Catal. Sci. Technol.*, 2025, **15**, 2571

Electrooxidation of ethylene glycol coupled with hydrogen production on porous NiO/Ni@NF nanosheet electrocatalysts†

Saba A. Aladeemy,[a] Toleen Rayid AlRijraji,[b] Mabrook S. Amer,[b] Prabhakarn Arunachalam *[b] and Abdullah M. Al-Mayouf *[b]

Electrooxidation of small organic compounds plays a crucial role in clean and efficient energy. This technology has the potential to transform waste materials into useful fuels and chemicals for renewable energy applications. Recently, ethylene glycol (EG) has gained considerable attention due to its high energy density, making it a great fuel for direct alcohol fuel cells. EG electrooxidation has attracted significant interest as an alternative hydrogen energy source to water splitting due to its sustainability and cost effectiveness. In this study, porous NiO/Ni_x@NF nanostructured catalysts were synthesized to enhance alkaline EG electrooxidation reactions. Electrodeposition was employed to grow these NiO/Ni_x structures on nickel foam (NF). The electrochemical characterization results indicate that the porous NiO/Ni_x@NF catalyst exhibits an onset potential of 1.3 V *vs.* RHE for the electrochemical oxidation of EG in a 1.0 M KOH solution. Additionally, this electrocatalyst has a maximum electrocatalytic activity of 121.6 mA cm^{-2}, 4.5 times greater than that of the bare Ni@NF catalyst (27.2 mA cm^{-2}). Moreover, Ni/NiO@NF demonstrated excellent electrocatalytic performance for both cathodic and anodic reactions, including EG electrooxidation and hydrogen evolution reaction (HER). The developed NiO/Ni_x@NF materials catalyzed EG electrolysis with a faradaic efficiency of 45.5%, demonstrating their ability to facilitate electrolysis. The electrocatalytic activity of NiO/Ni_x@NF porous catalyst toward EG is adequate and stable. Therefore, it appears to be a promising option for using EG in fuel cells.

Received 1st December 2024,
Accepted 22nd February 2025

DOI: 10.1039/d4cy01450b

rsc.li/catalysis

Introduction

The global energy crisis, rapid oil depletion, and pollution caused by the use of fossil fuels all encourage the development of environmentally friendly and sustainable energy sources.[1,2] Over the last few years, fuel cells have gained considerable attention as an effective energy and contamination solution.[3,4] In portable and mobile applications, direct alcohol fuel cells (DAFCs) have drawn substantial interest because of their high energy density and efficiency, being an innovative green energy technology that produces electrical energy directly from alcohol fuel chemical energy.[5] Furthermore, a DAFC uses liquid and renewable alcohol fuels to power its facilities, which are easy to store and transport.[6,7] Meanwhile, hydrogen is set to become an attractive cleaner fuel for a wide range of industries in the near future. Various methods can be used to produce green hydrogen, including electrocatalytic water splitting, photocatalytic water splitting, and photoelectrocatalytic water splitting.[8–10] The electrooxidation of ethylene glycol (EGOR) is a significant area of research owing to its potential applications in DAFCs and other electrochemical systems.[11–15] The process involves the conversion of EG into useful products such as hydrogen and carbon dioxide through electrochemical reactions.[16,17] However, there are several challenges to overcome before DAFC technology can be widely implemented. EGOR is hindered by the cost of catalysts and materials, which can affect the commercial viability of the process.

Platinum (Pt) is currently the best electrocatalyst for the oxidation of EG, but high cost, unstable properties, and low toxicity resistance have severely hindered its commercialization.[18,19] Numerous studies have been carried out to boost the electrocatalytic features and durability of Pt catalysts in alcohol electrooxidation.[20,21] Further, Bambagioni *et al.* examined EGOR on smooth and nanostructured Pd electrodes, noting that the pH of the solution significantly effects the reaction products, with different species being formed at varying pH levels.[22] A study by Murawska *et al.*

---

[a] *Department of Chemistry, College of Science and Humanities in Al-Kharj, Prince Sattam Bin Abdulaziz University, Al-Kharj 11942, Saudi Arabia*

[b] *Electrochemical Sciences Research Chair (ESRC), Chemistry Department, College of Science, King Saud University, P.O. Box 2455, Riyadh 11451, Saudi Arabia. E-mail: parunachalam@ksu.edu.sa, amayouf@ksu.edu.sa*

† Electronic supplementary information (ESI) available. See DOI: **https://doi.org/10.1039/d4cy01450b**

revealed that PtIr nanoparticles decorated with tungsten oxide exhibited higher catalytic activity for EGOR than traditional PtIr catalysts.[23] In recent years, EG has become popular as a way to generate hydrogen fuel in fuel cell-based EG with highly active Pt-based catalysts. For instance, Liu *et al.*[24] have developed core–shell Au–Pd@Pd NCs and employed them for EGOR in alkaline media. According to electrochemical results, the as-made Au–Pd@Pd NCs reveal an improvement in the anodic EG oxidation current (91.10 mA cm^{-2}) which is superior to that of Pd black (32.63 mA cm^{-2}). The authors noted that the inclusion of Au into the crystal Pd lattice enhanced hydroxyl ion adsorption onto the Au–Pd@Pd nanocrystals, their resistance to intermediate species, and their ability to catalyze EG reactions (a synergetic effect). In related work, Qi *et al.*[25] reported that PdAg/CNT catalysts achieved higher mass activity (2.105 mA μg_{Pd}^{-1}) than Pd/CNT catalyst for EGOR in 1.0 M KOH containing 0.1 M EG. These results point out that Ag metal revealed excellent activity toward the intermediate aldehyde oxidation, improving the fuel efficiency of EG oxidation. However, these catalysts suffer from several obstacles including their propensity to poisoning by CO-like intermediate products, the high cost and the scarcity of global resources, restricting the feasible implementation of direct fuel cells in commercial settings.[26,27] It is therefore mandatory to develop an economical, abundant, highly efficient and durable alternative catalyst for EGOR. Thus, it is beneficial to investigate non-Pt based electrocatalysts that exhibit superior conductivity and catalytic activity in order to reduce catalyst costs without compromising performance.[28] Therefore, nickel-containing materials have attracted significant attention for EG oxidation reactions due to their electrochemical properties, cost-effectiveness, and abundance.[29,30] Li *et al.* have demonstrated the selective oxidation of EG to formate using nickel selenides with different morphologies.[29] According to *in situ* infrared absorption spectroscopy and *ex situ* NMR analysis, the as-obtained nickel selenide catalyst leads to formate with up to 80% FE representing the main product of EG oxidation reactions in alkaline medium; glycolate and oxalate are also formed as by-products. Their findings suggest that electrode materials can be optimized to improve electrooxidation efficiency. Based on these results, we conclude that EGOR is a multifaceted process that depends on a number of factors, including the catalyst composition, the structure, and the electrochemical environment. Efforts are being made to develop more efficient, stable, and cost-effective catalysts to facilitate EG's practical application in fuel cells. Consequently, it is urgent to explore high performance transition metal-based catalysts with high electroactivity, selectivity, and stability for EG oxidation reactions to enhance reaction efficiency and reduce chemical and hydrogen fuel production costs.

Herein, porous metal nickel nanostructured electrocatalysts were electrodeposited using a potentiodynamic deposition process on NF. This novel approach leverages nickel-based electrocatalysts' unique properties to improve EGOR efficiency. It is possible to precisely control the porosity and surface area of nickel nanostructures using electrodeposition, enhancing their catalytic activity. In alkaline conditions, porous NiO/Ni_x@NF electrode materials were successfully fabricated using nickel chloride (nickel precursor) and dimethylsulphoxide (DMSO) as the complexing agent and solvent for EGOR. To prepare electrodes, DMSO is used as a complexing agent and solvent to dissolve and distribute the nickel precursor. During electrodeposition, this results in well-structured porous nickel nanostructures. Samples were characterized using a variety of electrochemical and physicochemical methods. Porous NiO/Ni_x@NF electrodes showed excellent electrocatalytic activity and stability, showing that they could function as high-performing catalysts for EG oxidation. The resultant NiO/Ni_x@NF exhibits extremely high stability over time, demonstrating advanced electrocatalysis for oxidation of liquid fuels.

Experimental section

Chemicals

Anhydrous nickel chloride, $NiCl_2$ (99.0%), was purchased from Alfa Aesar. The organic DMSO solvent (100.0%) was purchased from BDH. EG was purchased from Honeywell ($C_2H_4(OH)_2$, 99.5%). Nitric acid (HNO_3, 69%) was brought from AppliChem Panreac. Potassium hydroxide pellets (85.0%) were purchased from AnalaR Group. We utilized NF substrates obtained from the Zopin Group as working electrodes. We used deionized (DI) water (18 MΩ resistivity) throughout this study, which was obtained with a Milli-Q ultrapure water purification system. We used all chemicals as received.

Catalyst synthesis

The porous metal nickel nanostructured electrocatalysts were electrodeposited *via* potentiodynamic deposition on NF substrate using a Biologic potentiostat station. The conventional three-electrode cell consisted of commercial NF (1.0 × 2.0 cm^2), Ag/AgCl (3.0 M KCl) and another blank NF as the working, reference and counter electrodes, respectively. By sonification, NF was cleaned in 3.0 M HCl, DI water, and absolute ethanol for 15 minutes. The electrode was dried at 60 °C for 12 hours prior to use. In a typical process, the working electrode is immersed in DMSO solution containing 0.035 M $NiCl_2$. Before electrodeposition, nitrogen was bubbled continuously throughout the electrolyte solution for at least 30 minutes. Electrodeposition was performed *via* cyclic voltammetry (CV) within a potential of consecutive linear scans between −0.2 and 1.3 V *vs.* RHE at a sweep rate of 5 mV s^{-1} for different numbers of cycles (8, 12, and 16) at a reaction temperature at 62–64 °C to obtain the Ni nanostructures anchored on NF, which were categorized as NiO/Ni-8@NF, NiO/Ni-12@NF, and NiO/Ni-16@NF, respectively. After deposition, the NiO/Ni_x@NF electrodes were removed from the deposition bath and rinsed with water. Finally, they were dried in an oven at 60 °C for 12 h. For comparison, the electrodeposition process was also carried out using NF electrodes from DMSO solution without $NiCl_2$ source which was labeled as NiO/Ni-0@NF electrode.

Characterization

By using a MiniFlex-600 (Rigaku), we examined the crystal structure of the developed electrode materials at 40 kV and 15 mA with Cu Ka radiation. A field-emission scanning electron microscope (FE-SEM) operating at 15 kV and equipped with an energy-dispersive X-ray spectroscopy (EDS) analyzer was utilized to investigate catalyst morphology. An Escalab 250 spectrometer (Thermo-Fisher Scientific) was used to observe surface chemical states with X-ray photoemission spectroscopy (XPS). By using a Biologic potentiostat, which is controlled by EC-lab software, electrochemical measurements, CV and chronoamperometry (CA) were conducted. In EGOR tests, a three-electrode system was applied with catalysts deposited on NF substrates as working electrode (1.0 cm^2), graphite as counter electrode (1.0 cm^2), and Ag/AgCl reference electrode. For EGOR, the electrolyte was 1.0 M KOH in 0.03 M EG. An Agilent GC 8860 gas chromatography (GC) system was applied to evaluate the gaseous products. Using a thermal conductivity detector (TCD), H_2 was measured.

Results and discussion

Catalyst characterization

By potentiodynamic deposition, NiO/Ni$_x$-incorporated NF catalytic materials were fabricated in DMSO solution containing anhydrous $NiCl_2$. As shown in Fig. 1, NiO/Ni$_x$ catalytic materials are prepared on NF. NF was coated with NiO/Ni$_x$ active materials obtained by successive linear scanning and subsequently labelled NiO/Ni-0@NF, NiO/Ni-8@NF, NiO/Ni-12@NF, and NiO/Ni-16@NF. The linear scans of NiO/Ni-12@NF shown in Fig. S1† depict oxidation and reduction peak locations in the potential range of +0.3 to −1.25 V *vs.* RHE. The peaks are caused by the oxidation of nickel ions to form metallic nickel films on NF. Further, peak current upsurges with an increase in the number of cycles, and nickel amounts increase with an increase in NiO/Ni$_x$@NF film ratios. It should be noted that after several cycles, the exposed area of NF changes from silver to black.

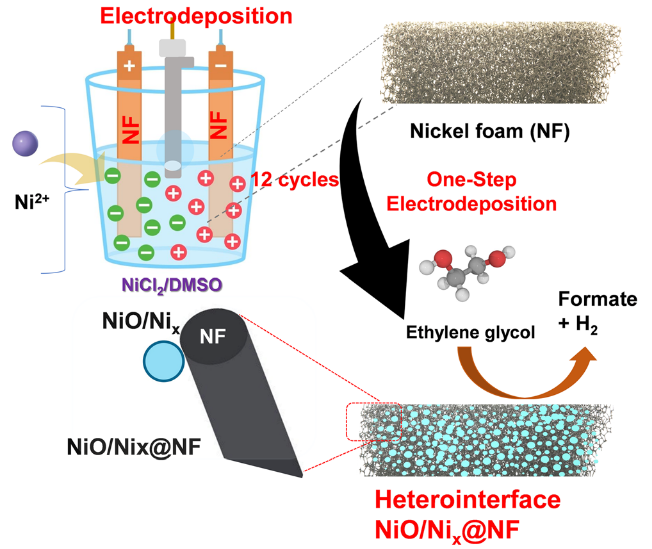

Fig. 1 Schematic diagram of electrodeposition procedures for porous NiO/Ni-0, NiO/Ni-8, NiO/Ni-12, and NiO/Ni-16 films grown on NF substrate.

Fig. 2a shows the XRD patterns obtained by probing a sequence of as-synthesized NiO/Ni$_x$ and Ni films grown on NF substrates. Based on the XRD analysis, several peaks were detected, corresponding to the diffractions of the (111), (200), and (220) planes of the NF substrate. Metallic nickel atoms interact with each other and are incorporated into the NF lattice to explain these peaks. Ni was deposited on NF substrates, resulting in broad diffraction peaks (Fig. 2b). Furthermore, there are two weak peaks at 49.9° and 73.71°, which can be attributed to NiO/Ni$_x$ decorations on NF prepared in various ways.[31–33] By adding NiO/Ni$_x$ decorations to the NF lattice, overall stability and electrical conductivity are enhanced. This could lead to increased conductivity and better catalytic performance in applications such as energy storage and conversion. XPS was also conducted on NiO/Ni-12@NF to further examine the surface composition and valence state. On the NF surface, Ni and O elements were scanned separately to demonstrate their uniform distribution. Notably, Ni, O and C contents in NiO/Ni-12@NF materials were assessed to be 10.27, 40.5 and 49.23 at%, respectively (Table S1†). It can be seen in Fig. 2c that Ni 2p peaks are clearly visible in the observed region. In the Ni $2p_{3/2}$ region, an XPS spectrum with two peaks correlates with binding energies (Bes) of 856.43 and 862.3 eV. As for the Ni $2p_{1/2}$ region, two peaks can be deconvoluted into 873.8 and 880.3 eV BEs (Fig. 2c), signifying that Ni exists in NiO/Ni-12@NF as Ni^{2+}.[34,35] Fig. 2d displays the high-resolution XPS spectrum of O element. It shows that the lattice oxygen of Ni–O and O–H can each be resolved into two peaks at about 533.4 and 532.1 eV.[36,37]

FE-SEM and transmission electron microscopy (TEM) methods were used to examine the morphological features of NF and NiO/Ni-12@NF. A FE-SEM image of a bare NF electrode is shown in Fig. 3 and images after NiO/Ni$_x$ hybrid nanostructures were electrodeposited in DMSO with different concentrations of anhydrous $NiCl_2$. The FE-SEM image of NF revealed a highly porous structure with interconnected networks, providing a large surface area (Fig. 3a and b). After electrodeposition of Ni, the SEM images showed that the NiO/Ni hybrid nanostructures were successfully immobilized on the NF surface (Fig. 3c–f). The surface of NF becomes rough after NiO/Ni-12 nanosheet formation, as seen in Fig. 3c–f, showing the growth of NiO/Ni-12 nanosheets over a significant region. A high-magnification SEM image taken from Fig. 3f shows that the 3D dendritic NiO array consists of many nanosheets with

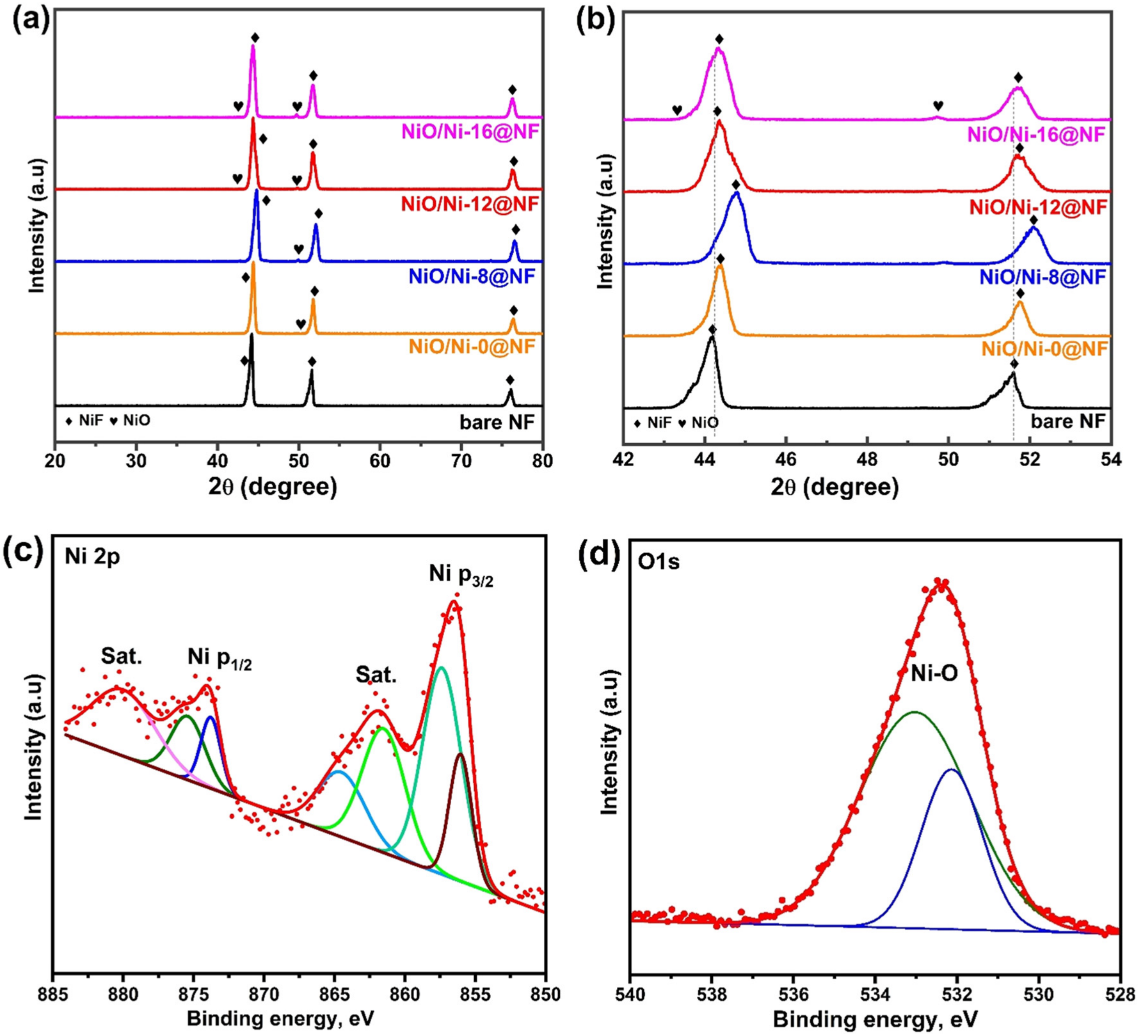

Fig. 2 (a) Normalized XRD patterns of the as-deposited NiO/Ni-0, NiO/Ni-8, NiO/Ni-12, and NiO/Ni-16 catalysts loaded on NF substrates prepared by electrodeposition approach. Diffraction peaks are indexed using reference peaks. (b) Enlarged view of as-deposited NiO/Ni-0, NiO/Ni-8, NiO/Ni-12, and NiO/Ni-16 catalysts. (c and d) High-resolution XPS spectra for Ni 2p and O 1s analysis of NiO/Ni-12@NF prepared by electrodeposition approach.

microscale diameters and nanoscale thicknesses. Moreover, Fig. S2† shows the EDS elemental analysis by means of the related SEM images for the NiO/Ni-12 nanosheet film. The EDS spectrum confirms the presence of Ni and O at an atomic ratio of 80.33 and 19.67 at%.

TEM was used to inspect the microstructure of mesoporous NiO/Ni-12@NF nanosheets. Fig. 4a–c display low-magnification TEM images of a NiO/Ni-12@NF nanosheet. These images reveal a uniform and well-defined mesoporous structure, with interconnected pore channels throughout the nanosheet. The interconnected pores increase the surface area of the material, which gives it a greater catalytic and adsorption capacity. They also facilitate efficient mass transport, allowing reactants and products to move through the material more easily during chemical reactions. The mesoporous structure of this nanosheet is formed by nickel nanoparticles with diameters of 10–30 nm and is coated with thin layers of amorphous NiO. The mesoporous nature of the NiO/Ni-12@NF nanosheets contributes to their high surface area, which is beneficial for applications requiring efficient mass and charge transport. Additionally, the nanosheets display a consistent thickness, further indicating the precision of the synthesis process.

Electrochemical characterization

The electrochemical behaviors of the bare NF substrate and all as-deposited porous NiO/Ni$_x$@NF nanostructured catalysts were first examined, being activated in a 1.0 M KOH solution, *via* CV measurements. Fig. 5a displays the CV analysis of fabricated films in 1.0 M KOH. In Fig. 5a, two distinct redox peaks are evident, which are attributed to the Ni(II)/Ni(III) redox couple.[38,39] An anodic peak at 1.43 V observed in the forward sweep indicates $Ni(OH)_2$ oxidation to NiOOH. A similar reduction of NiOOH to $Ni(OH)_2$ is responsible for the cathodic peak recorded at 1.25 V in the backward direction.

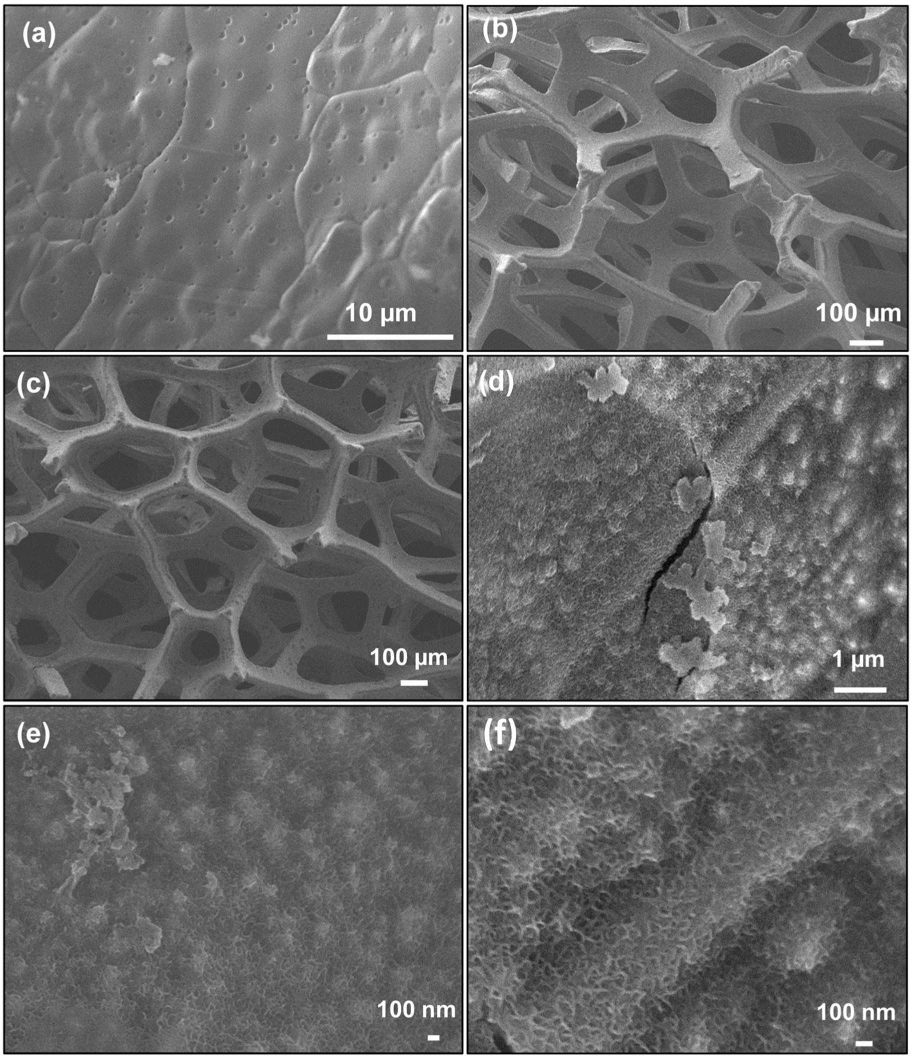

Fig. 3 Morphological characteristics of catalysts. (a and b) FE-SEM images of bare NF substrate, and (c–f) FE-SEM images of fabricated NiO/Ni-12@NF catalyst.

Generally, OER is associated with higher electrocatalytic currents at higher applied potentials. In Fig. 5a, OER onset potentials occur as follows: NiO/Ni-12@NF (360 mV), NiO/Ni-8@NF (370 mV), NF (390 mV), and NiO/Ni-16@NF (440 mV), demonstrating that NiO/Ni deposition over NF reduces OER overpotentials. Consequently, NiO/Ni-12@NF had the best performance, signifying a rapid reaction rate and maintaining an optimal current density of 1.50–1.80 V_{RHE}. On NF substrates, electrodeposition cycles (NiO/Ni-16@NF) reduced electrocatalytic features. As seen with NiO/Ni-16@NF, electrocatalytic performance declines with increasing deposition cycles. This can be attributed to the thicker NiO/Ni layers, which may hinder charge transfer and reduce the active surface area available for the reaction. In turn, these electrocatalytic properties of NiO/Ni-12@NF have been attributed to optimized NiO/Ni concentrations in surface-active regions of NF, resulting in high electron transfer and sorption of OER intermediates.

In order to conduct a more comprehensive analysis of the catalytic properties of the as-made catalysts, CV tests were executed in 0.03 M EG in 1.0 M KOH, as shown in Fig. 5b. We have chosen these electrolytes (1.0 M KOH/0.03 M EG) based on their proven effectiveness in promoting the ionic conductivity and overall features of the electrolyte solution. Specifically, KOH is known for its high ionic conductivity, while EG acts as a stabilizing agent, improving the stability and efficiency of the electrolyte. The combination has been validated by previous research[30] and experimental data, which show optimal performance in our studies. Fig. 5b illustrates the existence of two distinct peaks observed across all CV curves. In the case of the NiO/Ni-12@NF catalyst, the dominant peak located at 1.60 V during the forward scan is indicative of EG oxidation. As a result, the peak at 1.64 V observed during the reverse scan is less pronounced, which is due to partially oxidized carbonaceous species being removed during the reverse sweep.[40,41] The forward peak current density (j_f) for the NiO/Ni-12@NF catalyst is about

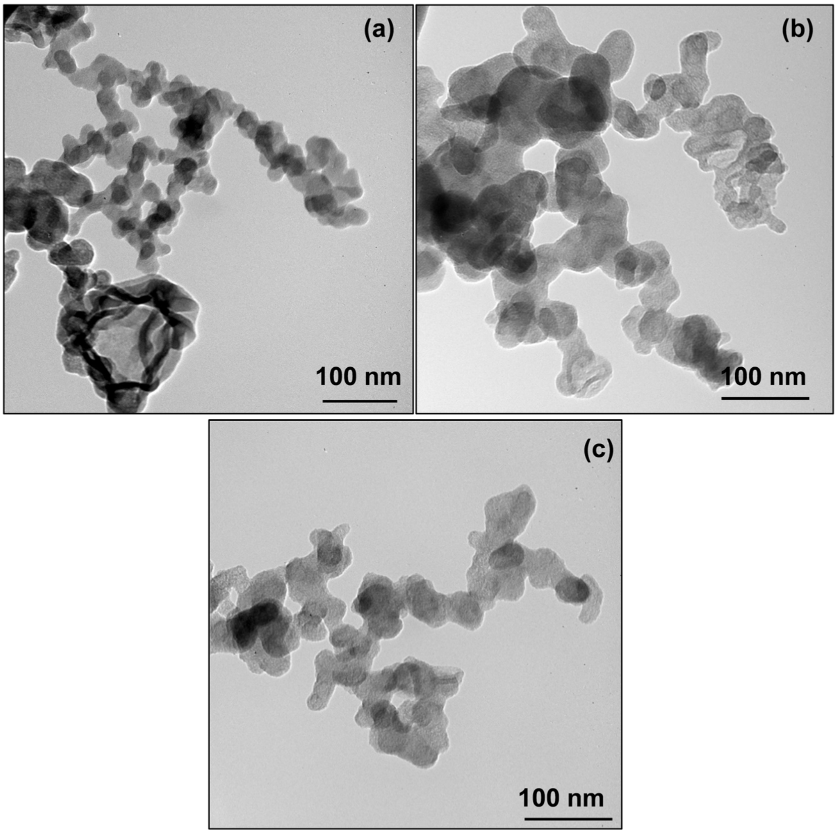

Fig. 4 (a–c) Low-magnification TEM images of as-deposited NiO/Ni-12@NF catalyst prepared by electrodeposition approach.

121.6 mA cm^{-2} at 1.60 V *vs.* RHE, which is around 4.5 times greater than that of NiO/Ni-0@NF (27.2 mA cm^{-2}), and 1.5 times larger than that of NiO/Ni-8@NF (87.9 mA cm^{-2}). These findings highlight the improved catalytic activity of the NiO/Ni-12@NF catalyst compared to its counterparts. The significantly higher forward peak current density indicates a more efficient oxidation process, which could lead to improved performance in electrochemical applications.

In Fig. 5c, we observe a sharp upsurge in anodic current density after the introduction of EG solution for the porous NiO/Ni-12@NF catalyst at the same potential (1.33 V *vs.* RHE) which indicated that NiOOH is the primary form of EGOR in alkaline media.[29] Based on these findings, EGOR occurs when EG adsorbs at the surface of the NiO/Ni-12@NF catalyst, forming glycollates.[30] Moreover, as previously discussed, the reverse oxidation peak at an overpotential of 1.64 V *vs.* RHE can be explained by the electrooxidation of glycollate into oxalate, as described in eqn (5) and (6). According to the reported literature,[30,42] and the obtained CV results discussed above, a potential mechanism for the electrooxidation of EG in alkaline media on the surface of the nickel-based catalysts can be suggested in terms of eqn (1)–(6). The proposed mechanism suggests that the developed catalysts oxidize EG into oxalate, which can then be further catalyzed by OH^- ions. The reverse oxidation peak has a lower overpotential than the forward oxidation peak, which supports this mechanism.

$$\mathrm{Ni(OH)_2 + OH^- \rightarrow NiOOH + H_2O + e^-} \tag{1}$$

$$\mathrm{(CH)_2(OH)_2 + Ni^{2+} \rightarrow Ni^{2+}\text{–}(OHCH_2CH_2OH)_{ads}} \tag{2}$$

$$\mathrm{2NiOOH + Ni^{2+}\text{–}(OHCH_2CH_2OH)_{ads} \rightarrow 2Ni(OH)_2 + Ni^{2+}\text{–}(OHCH_2CHO)_{ads}} \tag{3}$$

$$\mathrm{2NiOOH + OH^- + Ni^{2+}\text{–}(OHCH_2CHO)_{ads} \rightarrow 2Ni(OH)_2 + Ni^{2+}\text{–}(OHCH_2COO^-)_{ads}} \tag{4}$$

$$\mathrm{2NiOOH + Ni^{2+}\text{–}(OHCH_2COO^-)_{ads} \rightarrow 2Ni(OH)_2 + Ni^{2+}\text{–}(CHOCOO^-)_{ads}} \tag{5}$$

$$\mathrm{2NiOOH + 3OH^- + Ni^{2+}\text{–}(CHOCOO^-)_{ads} \rightarrow 3Ni(OH)_2 + Ni^{2+}\text{–}(^-OOCCOO^-)_{ads}} \tag{6}$$

In the non-Faradic zone, the electrochemical surface area (ECSA) values of as-made NiO/Ni-8@NF, NiO/Ni-12@NF, and NiO/Ni-16@NF catalysts were determined using CV curves obtained at different sweep rates (Fig. S3, ESI†). In Fig. 5d, the C_{dl} in 1.0 M KOH was recorded at various scan rates between 40 mV and 150 mV, according to the following equation: ECSA = C_{dl}/C_s, where C_s refers to the specific capacitance equal to 0.04 mF cm^{-2} in aq. 1.0 M KOH. The ECSA for NiO/Ni-8@NF, NiO/Ni-12@NF, and NiO/Ni-16@NF catalysts are 3.86 (96.5 cm^2), 5.97 (149.3 cm^2), and 3.02 mF (75.5 cm^2), respectively. Prepared porous NiO_x nanosheets

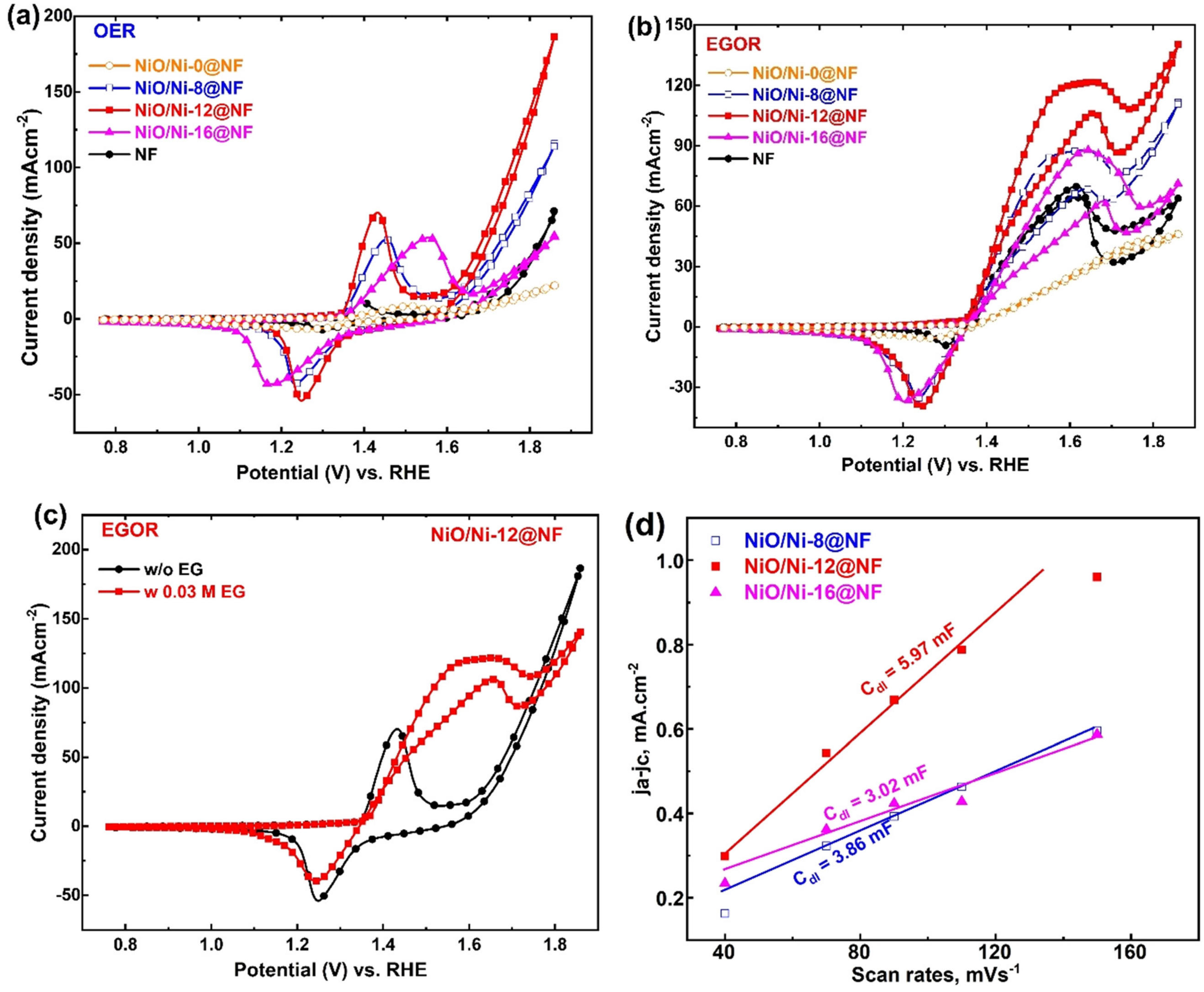

Fig. 5 Electrochemical oxidation of EG. (a) CV of as-deposited NiO/Ni-0@NF, NiO/Ni-8@NF, NiO/Ni-12@NF, and NiO/Ni-16@NF catalysts at 50 mV s^{-1} in 1.0 M KOH. (b) CV of all samples in 0.03 M EG dissolved in KOH. (c) CV of NiO/Ni-12@NF and NiO/Ni-0@NF catalysts in 0.03 M EG/KOH. (d) Capacitive currents of NiO/Ni-8@NF, NiO/Ni-12@NF, and NiO/Ni-16@NF catalysts.

possess bifunctional features, enabling them to facilitate both EGOR and OER. These bifunctional features make NiO_x nanosheets highly efficient catalysts for energy conversion processes. Their ability to enhance both oxidation and oxygen evolution reactions can significantly improve the performance of hydrogen production systems, making them a promising material for advancing clean energy technologies. Consequently, the porous NiO/Ni-12@NF catalyst has more active sites than the other catalysts, making it easier for EG to move into the porous structure's inner surface area. Table 1 compares our findings with those published in the scientific literature in order to gain a

Table 1 Comparison of the EGOR features of our catalysts with those of described active noble metal-based catalysts in alkaline medium

Catalyst	Onset potential, V	Current density, mA cm^{-2}	Stability, s	Substrate	Ref.
$NiSe_2$-branched particles	1.59 V *vs.* RHE	95.23	—	1.0 M EG/1.0 M KOH	29
Au–Pd@Pd NCs	−0.49 V *vs.* SCE	91.10	5000	0.5 M EG/10.5 M KOH	24
PtRuPd NSs		116.11		0.5 M EG/0.5 M KOH	43
NiNPs/ITO	0.42 V *vs.* Ag/AgCl	1.0	300	0.03 M EG/0.2 M NaOH	30
Pd/C-CeO_2	−0.37 V *vs.* Hr/HgO	68.5	4000 s	1.0 M EG/1 M KOH	44
Spinel $NiMn_2O_4$	0.10 V *vs.* Ag/AgCl	24	10 h	1.0 M EG/1 M KOH	45
PdCu-H HNCs	0.4 V *vs.* RHE	100 @ 0.808 V *vs.* RHE	12 h	1.0 M EG/1 M KOH	46
Porous NiO/Ni-12@NF	1.33 V *vs.* RHE	121.6 @ 1.6 V *vs.* RHE	3600 s	0.03 M EG/1.0 M KOH	This work

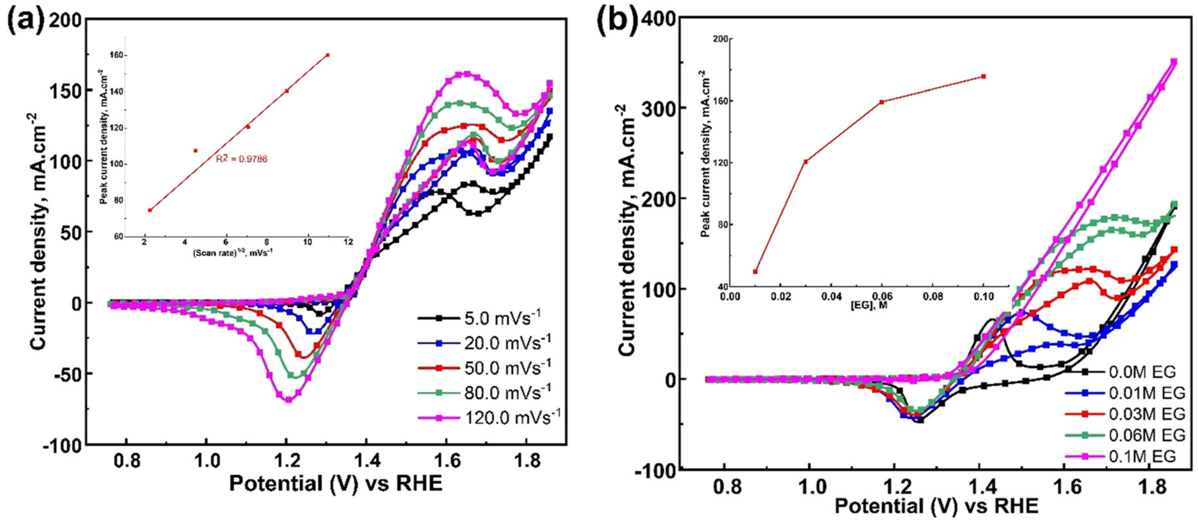

Fig. 6 (a) CV of as-deposited NiO/Ni-12@NF catalyst in 0.03 M EG/KOH at various scan rates. The inset shows a plot of current *vs.* square root of the sweep rate. (b) CV of as-deposited NiO/Ni-12@NF catalyst in 0.03 M EG/KOH at various EG concentrations. The inset shows a plot of current *vs.* EG concentrations.

comprehensive understanding of the electrochemical efficiency of our porous NiO/Ni-12@NF catalyst in an alkaline electrolyte. As compared with noble metal-based catalysts, the porous NiO/Ni-12@NF catalyst had exceptional catalytic performance in the EGOR process.

CV responses were measured at various sweep rates to study the mechanism of EGOR transfer through the NiO/Ni-12@NF porous catalyst. Fig. 6a shows the CV plots of NiO/Ni-12@NF-catalyzed EGOR in 1.0 M KOH with 0.03 M EG at sweep rates varying from 5 to 120 mV s^{-1}. As the sweep rate upsurges, the redox currents rise gradually. The linear association between the peak anodic current and the square root of the potential scan rate (inset plot in Fig. 6a) suggests that diffusion controls the EGOR on NiO/Ni-12@NF. Furthermore, EG concentrations were investigated to determine their effect on EGOR performance. The CV plots are shown in Fig. 6b for the NiO/Ni-12@NF catalyst with different amounts of EG (0.01–0.10 M). As the concentration increased, the anodic current increased as well. Fig. 6b illustrates the linear relationship between EG amounts in KOH and oxidation peak currents. Diffusion-controlled processes appear to be important at EG concentrations between 0.01 and 0.10 M. It is evident from the figure that EG oxidation can be effectively catalyzed by NiO/Ni-12@NF.

CA was used to further evaluate the EGOR performance of the NiO/Ni$_x$@NF porous catalysts at 1.5 V for 3600 s in 0.03 M EG/KOH (Fig. 7a). Clearly, the oxidation current density is much higher for the NiO/Ni-12@NF catalyst than for the other catalysts, and it decreases for the NiO/Ni-12@NF catalyst at a slower rate throughout the measurement. During EGOR, intermediate products that are similar to CO are produced.[40,47] Based on these findings, the NiO/Ni-12@NF catalyst shows better EGOR activity than NiO/Ni-0@NF, NiO/Ni-8@NF, or NiO/Ni-16@NF catalysts, confirming that the NiO/Ni-12@NF catalyst has more active sites for enhancing EGOR. For studying EGOR processes, electrochemical impedance (Fig. 7b and c) provides an excellent way to study interfacial kinetics and charge resistance. As shown in Fig. 7b, EGOR over the NiO/Ni-12@NF catalyst in 1.0 M KOH containing 0.03 M EG was analyzed with Nyquist plots and equivalent circuits at 1.36, 1.46, and 1.51 V. Fig. 7b shows that the NiO/Ni-12@NF catalyst has the same impedance arc across all frequencies. In particular, NiO/Ni-12@NF reveals the smallest impedance arc radius in the higher frequency region, likely due to the charge transfer resistance characteristic of EG oxidation ($Ni(OH)_2$/NiOOH electroactive sites). Also, at all applied potentials, a large semicircle represents the adsorption process of the intermediates in the low-frequency zone. As the oxidation potential increases from 1.36 to 1.51 V_{RHE}, the charge transfer R_2 significantly increased, indicating that the electrocatalytic EG oxidation was improved at higher potentials, in accord with the CV results. In Fig. 7b, the EIS plots of nickel catalysts shown can be modeled using the circuits shown in the inset. In Table 2, we list the parameters used to fit the equivalent circuit. These parameters include the electrolyte resistance (R_1), the charge transfer resistance (R_2), and the constant phase element (Q_2). Also, R_3 refers to the intermediate adsorption resistance and Q_3 is related to the adsorption capacitance of EG oxidation at $Ni(OH)_2$/NiOOH of as-made nickel catalysts. Fig. 7c shows EIS Nyquist plots of 0.03 M EG dissolved in 1.0 M KOH for the NiO/Ni-12@NF catalyst at 1.46 V *vs.* RHE. As can be seen, the NiO/Ni-12@NF catalyst has a much lower charge transfer resistance ($R_2 = 0.135\ \Omega$) than the NiO/Ni-0@NF catalyst ($R_2 = 3.333\ \Omega$) at 0.45 V, indicating that the EG oxidation reaction kinetics for the NiO/Ni-12@NF catalyst is much faster than for the NiO/Ni-0@NF catalyst.

EG's oxidation potential was assessed by linear sweep voltammetry (LSV). LSV was performed in a solution of 0.03 M EG and 1 M KOH. In Fig. 8a, onset potential is

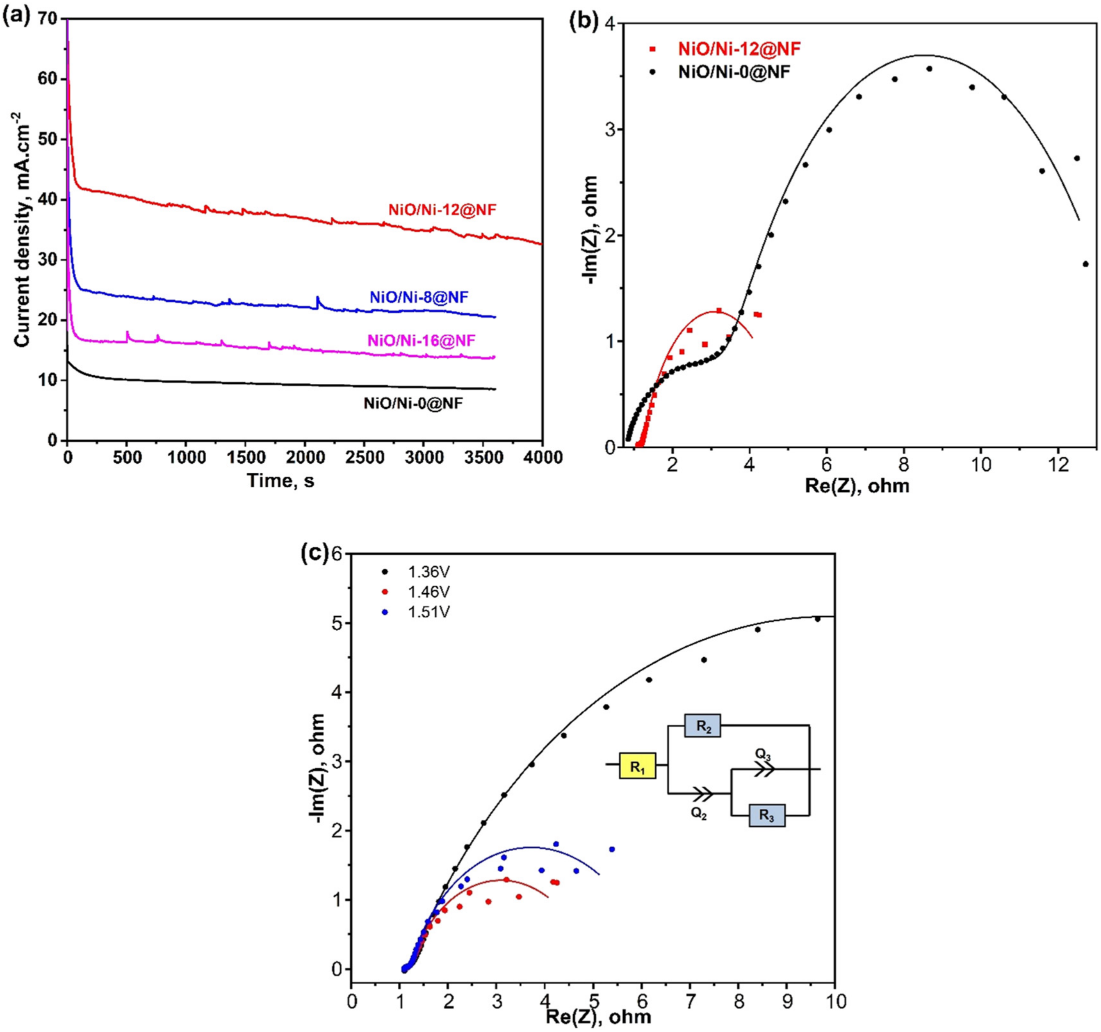

Fig. 7 (a) Time-dependent current density plots of as-deposited NiO/Ni-0@NF, NiO/Ni-8@NF, NiO/Ni-12@NF, and NiO/Ni-16@NF catalysts recorded at 1.51 V *vs.* RHE. (b) Nyquist plots of NiO/Ni-12@NF and NiO/Ni-0@NF catalysts at 1.46 V *vs.* RHE (inset shows an enlarged view in the high-frequency region). (c) Nyquist plots of NiO/Ni-12@NF catalyst at shown potentials (inset refers to the equivalent circuit model).

Table 2 EIS parameters of porous NiO/Ni-12@NF and NiO/Ni-0@NF catalysts recorded through fitting EIS spectra measured at 450 mV

Material	R_1, ohm	Q_2 (F sn^{-1})	R_2, ohm	Q_3 (F sn^{-1})	R_3, ohm
NiO/Ni-12@NF at 1.36 V	1.184	0.0608	0.8279	25.76×10^{-15}	16.46
NiO/Ni-12@NF at 1.46 V	1.105	0.0203	0.1356	0.1055	3.759
NiO/Ni-12@NF at 1.51 V	1.10	0.0216	0.1482	0.1011	4.032
NiO/Ni-0@NF at 1.46 V	0.748	0.0051	3.333	0.0168	10.11

shown to be 1.84 volts for a 1 M KOH solution, which agrees to the point at which water breakdown occurs. In the presence of EG, on the other hand, there is an onset potential of 1.47 V. LSV data obtained in the present study indicate decreased EG initiation potentials. The water decomposition in Fig. 8a is further accelerated by a 10 mA cm^{-2} current density. The overpotential of EG at this point was 1.59 V lower than the overpotential of water decomposition, which was 1.85 V. In this case, the presence of EG led to a reduction in the voltage required for the oxidation reaction to take place. The hydrogen evolution rate (HER) of EG electrolysis conducted with the NiO/Ni-12@NF catalyst was assessed in a solution containing 1.0 mol KOH and 0.03 mol EG. The GC technique is used in this study,[48,49] with NiO/Ni-12@NF anode (0.50 mg cm^{-2}) and a Pt electrode as a cathode. Using CA measurements, Fig. 8b shows the rate at which cathodic hydrogen is produced for a 1.7 V applied potential when 0.03 M EG is present. According to the findings, when using a 0.03 M EG solution and applying an overpotential of 1.7 V, the rate of hydrogen production at the cathode reaches 90.2 mmol h^{-1}.

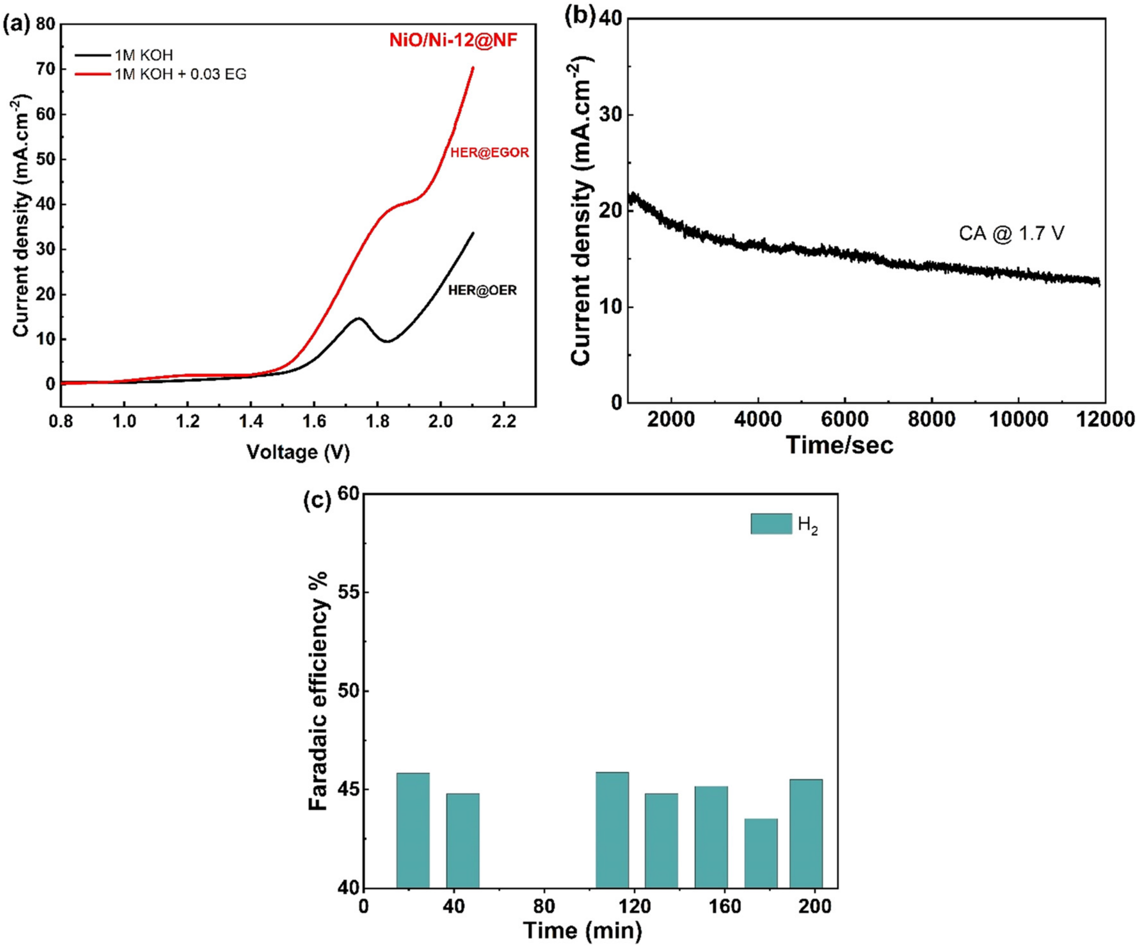

Fig. 8 (a) LSV of NiO/Ni-12@NF in the absence and presence of 0.03 M EG/1 M KOH in a two-electrode system. (b) CA of NiO/Ni-12@NF in 0.03 M EG/1 M KOH at an overpotential of 1.7 V. (c) Faradic efficiency of NiO/Ni-12@NF in 0.03 M EG/1 M KOH for hydrogen production.

Further, the faradaic efficiency (Fig. 8c) achieved when using the NiO/Ni-12@NF catalyst in combination with EG electrolysis was 45.5%, demonstrating its high energy efficiency and cost-effectiveness. In this context, a faradaic efficiency of 45.5% indicates that nearly half of the applied electrical energy is used to produce hydrogen, highlighting the efficiency of the NiO/Ni-12@NF catalyst in facilitating EG electrolysis. In a faradaic process, 45.5% of the input energy is utilized for hydrogen production, which minimizes waste and improves overall sustainability. This efficiency is particularly important for energy conversion technologies, where maximizing energy use translates into cost savings and reduced environmental impact. The high faradaic efficiency, namely 45.5%, indicates that the catalyst is highly effective at converting electrical energy into chemical energy. Overall, these results indicate that NiO/Ni-12@NF is a promising candidate for EG electrolysis.

Conclusion

In this study, an electrodeposition process was employed to grow a series of Ni_x films onto NF substrates, resulting in the creation of unique porous catalysts. The developed porous Ni electrocatalysts offer a large surface area that enhances chemical reaction rates by creating more active sites. The as-deposited NiO/Ni_x@NF catalysts facilitate EGOR through the catalytic activity of Ni(III) species present on the catalyst surface. These catalysts exhibit remarkable performance in EGOR, making them highly effective for applications in alkaline DAFCs. Electrocatalytic oxidation of EG in an alkaline solution was demonstrated to be highly efficient with the NiO/Ni_x@NF catalysts. Furthermore, CV and CA studies indicate that the NiO/Ni_x@NF catalysts under consideration are stable and have a high catalytic activity. Due to the synergistic effect between NiO and Ni_x, this exceptional performance is attributed to enhanced catalytic activity and stability. The two-electrode electrolyzer with NiO/Ni_x@NF catalysts and platinum plates as the anode and cathode for EGOR and HER is particularly promising with its 1.7 V potential to generate cathodic hydrogen at a current density of 20 mA cm^{-2} with a faradic efficiency of 45%. As a result, these catalysts have great potential for use in a wide range of electrochemical applications, especially in energy conversion and storage. The aforementioned findings indicate that the NiO/Ni$_x$@NF catalysts have significant potential as catalysts for fuel cells based on EG.

Data availability

The data supporting this article have been included as part of the ESI.†

Author contributions

Saba A. Aladeemy: conceptualization, data curation, formal analysis, investigation, writing – original draft. Toleen Rayid AlRijraji: formal analysis, investigation. Prabhakarn Arunachalam: writing – review & editing, data curation, supervision. Mabrook S. Amer: data curation, formal analysis, Abdullah M. Al-Mayouf: supervision, funding acquisition, project administration.

Conflicts of interest

The authors declare that they have no known competing financial interests or personal relationships that could have appeared to influence the work reported in this paper.

Acknowledgements

The authors are grateful to the Deanship of Scientific Research, King Saud University for funding through the Vice Deanship of Scientific Research Chairs; Electrochemical Sciences Research Chairs.

References

1 G. Zhang, *et al.*, Highly Active and Stable Catalysts of Phytic Acid-Derivative Transition Metal Phosphides for Full Water Splitting, *J. Am. Chem. Soc.*, 2016, **138**(44), 14686–14693, DOI: **10.1021/jacs.6b08491**.

2 A. Zalineeva, *et al.*, Self-supported PdxBi catalysts for the electrooxidation of glycerol in alkaline media, *J. Am. Chem. Soc.*, 2014, **136**(10), 3937–3945, DOI: **10.1021/ja412429f**.

3 D. Qazzazie, *et al.*, Platinum nanowires anchored on graphene-supported platinum nanoparticles as a highly active electrocatalyst towards glucose oxidation for fuel cell applications, *Nanoscale*, 2017, **9**(19), 6436–6447, DOI: **10.1039/c7nr01391d**.

4 H. Xu, *et al.*, Shape-Controlled Synthesis of Platinum-Copper Nanocrystals for Efficient Liquid Fuel Electrocatalysis, *Langmuir*, 2018, **34**(27), 7981–7988, DOI: **10.1021/acs.langmuir.8b01729**.

5 E. Antolini, Pt-Ni and Pt-M-Ni (M = Ru, Sn) anode catalysts for low-temperature acidic direct alcohol fuel cells: A review, *Energies*, 2017, **10**(42), 1–20, DOI: **10.3390/en10010042**.

6 S. P. S. Badwal, *et al.*, Direct ethanol fuel cells for transport and stationary applications - A comprehensive review, *Appl. Energy*, 2015, **145**, 80–103, DOI: **10.1016/j.apenergy.2015.02.002**.

7 H. Liu, *et al.*, A review of anode catalysis in the direct methanol fuel cell, *J. Power Sources*, 2006, **155**(2), 95–110, DOI: **10.1016/j.jpowsour.2006.01.030**.

8 S. Rajalekshmi, S. M. S. Kumar and A. Pandikumar, Exploring transition metal hydroxides performance in membrane-free electrolyzer based decoupled water splitting for step-wise production of hydrogen and oxygen, *Chem. Eng. J.*, 2024, **496**(15), 154215, DOI: **10.1016/j.cej.2024.154215**.

9 A. S. Darsan, *et al.*, From One-Pot to Powerhouse: Al–Fe2O3 Thin Films Coupled with Hexagonal ZnFe LDH for Water Oxidation in Alkaline Environment, Energy, *ACS Appl. Mater. Interfaces*, 2024, **16**(39), 52515–52528, DOI: **10.1021/acsami.4c12180**.

10 A. Sunny, S. Rajalekshmi and A. Pandikumar, Nanocomposite engineering: Tailoring MXene/Cobalt oxide for efficient electrocatalytic hydrogen and oxygen evolution reactions, *J. Alloys Compd.*, 2024, **1003**(25), 175532, DOI: **10.1016/j.jallcom.2024.175532**.

11 A. Marchionni, *et al.*, Electrooxidation of ethylene glycol and glycerol on Pd-(Ni-Zn)/C anodes in direct alcohol fuel cells, *ChemSusChem*, 2013, **6**(3), 518–528, DOI: **10.1002/cssc.201200866**.

12 Z. Pan, B. Huang and L. An, Performance of a hybrid direct ethylene glycol fuel cell, *Int. J. Energy Res.*, 2019, **43**(7), 2583–2591, DOI: **10.1002/er.4176**.

13 T. Hu, *et al.*, Construction of Pd-amorphous Fe2O3 interface for boosting selective electrooxidation of ethylene glycol, *Int. J. Hydrogen Energy*, 2025, **101**(3), 779–784, DOI: **10.1016/j.cej.2024.155924**.

14 Y. Wang, *et al.*, RhCo alloyed nanodendrites as an efficient electrocatalyst for boosting electro oxidation of ethylene glycol in alkaline media, *Chem. Eng. J.*, 2024, **499**(1), 155924, DOI: **10.1016/j.cej.2024.155924**.

15 D. Jang, *et al.*, Structural Modification Effect of Se-doped Porous Carbon for Hydrogen Evolution Coupled Selective Electrooxidation of Ethylene Glycol to Value-added Glycolic Acid, *Small*, 2024, **20**(49), 2404540, DOI: **10.1002/smll.202404540**.

16 A. Serov and C. Kwak, Recent achievements in direct ethylene glycol fuel cells (DEGFC), *Appl. Catal., B*, 2010, **97**(1–2), 1–12, DOI: **10.1016/j.apcatb.2010.04.011**.

17 R. B. De Lima, *et al.*, On the electrocatalysis of ethylene glycol oxidation, *Electrochim. Acta*, 2003, **49**(1), 85–91, DOI: **10.1016/j.electacta.2003.05.004**.

18 R. Kannan, *et al.*, Synchronized synthesis of PdC-RGO carbocatalyst for improved anode and cathode performance for direct ethylene glycol fuel cell, *Chem. Commun.*, 2014, **50**(93), 14623–14626, DOI: **10.1039/c4cc06879c**.

19 J. X. Tang, *et al.*, Screw-like PdPt nanowires as highly efficient electrocatalysts for methanol and ethylene glycol oxidation, *J. Mater. Chem. A*, 2018, **6**(5), 2327–2336, DOI: **10.1039/c7ta09595c**.

20 Y. Feng, *et al.*, 3D Platinum–Lead Nanowire Networks as Highly Efficient Ethylene Glycol Oxidation Electrocatalysts, *Small*, 2016, 4464–4470, DOI: **10.1002/smll.201601620**.

21 K. Spies and E. M. Stuve, Hydrogen Generation by Electrocatalytic Reforming of Ethylene Glycol on a Platinum Electrode, *ECS Trans.*, 2011, **35**(28), 31–35, DOI: **10.1149/1.3641816**.

22 V. Bambagioni, *et al.*, Ethylene glycol electrooxidation on smooth and nanostructured Pd electrodes in alkaline media, *Fuel Cells*, 2010, **10**(4), 582–590, DOI: **10.1002/fuce.200900120**.

23 M. Murawska, J. A. Cox and K. Miecznikowski, PtIr–WO3nanostructured alloy for electrocatalytic oxidation of ethylene glycol and ethanol, *J. Solid State Electrochem.*, 2014, **18**(11), 3003–3010, DOI: **10.1007/s10008-014-2493-0**.

24 Q. Liu, *et al.*, Simple wet-chemical synthesis of core–shell Au–Pd@Pd nanocrystals and their improved electrocatalytic activity for ethylene glycol oxidation reaction, *Int. J. Hydrogen Energy*, 2016, **41**(4), 2547–2553, DOI: **10.1016/j.ijhydene.2015.11.143**.

25 J. Qi, *et al.*, PdAg/CNT catalyzed alcohol oxidation reaction for high-performance anion exchange membrane direct alcohol fuel cell (alcohol = methanol, ethanol, ethylene glycol and glycerol), *Appl. Catal., B*, 2016, **199**, 494–503, DOI: **10.1016/j.apcatb.2016.06.055**.

26 P. Pattanayak, *et al.*, Fabrication of cost-effective non-noble metal supported on conducting polymer composite such as copper/polypyrrole graphene oxide (Cu2O/PPy–GO) as an anode catalyst for methanol oxidation in DMFC, *Int. J. Hydrogen Energy*, 2018, **43**(25), 11505–11519, DOI: **10.1016/j.ijhydene.2017.04.300**.

27 G. M. Tomboc, *et al.*, Utilization of the superior properties of highly mesoporous PVP modified NiCo2O4 with accessible 3D nanostructure and flower-like morphology towards electrochemical methanol oxidation reaction, *J. Energy Chem.*, 2019, 136–146, DOI: **10.1016/j.jechem.2018.08.009**.

28 B. Dong, *et al.*, Fabrication of hierarchical hollow Mn doped Ni(OH)2 nanostructures with enhanced catalytic activity towards electrochemical oxidation of methanol, *Nano Energy*, 2019, **55**, 37–41, DOI: **10.1016/j.nanoen.2018.10.050**.

29 J. Li, *et al.*, Selective Ethylene Glycol Oxidation to Formate on Nickel Selenide with Simultaneous Evolution of Hydrogen, *Adv. Sci.*, 2023, **10**(15), 2300841, DOI: **10.1002/advs.202300841**.

30 Q. Lin, *et al.*, Electrocatalytic oxidation of ethylene glycol and glycerol on nickel ion implanted-modified indium tin oxide electrode, *Int. J. Hydrogen Energy*, 2017, **42**(2), 1403–1411, DOI: **10.1016/j.ijhydene.2016.10.011**.

31 M. Huang, J. Ji and Y. Zhang, Facile synthesis of single-crystalline NiO nanosheet arrays on Ni foam for high-performance supercapacitors, *CrystEngComm*, 2014(16), 2878, DOI: **10.1039/c3ce42335b**.

32 G. Cheng, *et al.*, Nickel oxide nanopetal-decorated 3D nickel network with enhanced pseudocapacitive properties, *RSC Adv.*, 2015, **5**, 15042–15051, DOI: **10.1039/C4RA15556D**.

33 H. Faraji, K. Hemmati and K. Mirabbaszadeh, Nickel-based nanosheets array as a binder free and highly efficient catalyst for electrochemical hydrogen evolution reaction, *Int. J. Hydrogen Energy*, 2022, **47**(82), 34887–34897, DOI: **10.1016/j.ijhydene.2022.08.070**.

34 M. S. Amer, *et al.*, Facile synthesis of amorphous nickel iron borate grown on carbon paper as stable electrode materials for promoted electrocatalytic urea oxidation, *Catal. Today*, 2022, **397–399**, 197–205, DOI: **10.1016/j.cattod.2021.09.036**.

35 S. A. Aladeemy, *et al.*, Engineered CoS/Ni3S2 Heterointerface Catalysts Grown Directly on Carbon Paper as an Efficient Electrocatalyst for Urea Oxidation, *Catalysts*, 2024, **14**(9), 570, DOI: **10.3390/catal14090570**.

36 D. Zhao, *et al.*, Controllable construction of micro/nanostructured NiO arrays in confined microchannels via microfluidic chemical fabrication for highly efficient and specific absorption of abundant proteins, *J. Mater. Chem. B*, 2015, **3**(20), 4272–4281, DOI: **10.1039/c5tb00324e**.

37 S. A. Aladeemy, *et al.*, Electrooxidation of Urea in Alkaline Solution Using Nickel Hydroxide Activated Carbon Paper Electrodeposited from DMSO Solution, *Catalysts*, 2021, **11**(1), 102, DOI: **10.3390/catal11010102**.

38 M. A. Al-Omair, A. H. Touny and M. M. Saleh, Reflux-based synthesis and electrocatalytic characteristics of nickel phosphate nanoparticles, *J. Power Sources*, 2017, **342**, 1032–1039, DOI: **10.1016/j.jpowsour.2016.09.079**.

39 J. Meng, *et al.*, Self-supported Ni(OH)2/MnO2 on CFP as a flexible anode towards electrocatalytic urea conversion: The role of composition on activity, redox states and reaction dynamics, *Electrochim. Acta*, 2019, **318**, 32–41, DOI: **10.1016/j.electacta.2019.06.013**.

40 J. H. Kim, *et al.*, Influence of Sn content on PtSn/C catalysts for electrooxidation of C1-C3 alcohols: Synthesis, characterization, and electrocatalytic activity, *Appl. Catal., B*, 2008, **82**(1–2), 89–102, DOI: **10.1016/j.apcatb.2008.01.011**.

41 R. G. Da Silva, *et al.*, Insight into the Electrooxidation Mechanism of Ethylene Glycol on Palladium-Based Nanocatalysts: In Situ FTIRS and LC-MS Analysis, *ChemElectroChem*, 2020, **7**(21), 4326–4335, DOI: **10.1002/celc.202001019**.

42 L. An and R. Chen, Recent progress in alkaline direct ethylene glycol fuel cells for sustainable energy production, *J. Power Sources*, 2016, **329**, 484–501, DOI: **10.1016/j.jpowsour.2016.08.105**.

43 J. J. Duan, *et al.*, Porous dendritic PtRuPd nanospheres with enhanced catalytic activity and durability for ethylene glycol oxidation and oxygen reduction reactions, *J. Colloid Interface Sci.*, 2020, **560**, 467–474, DOI: **10.1016/j.jcis.2019.10.082**.

44 S. Sankar, *et al.*, Electro-oxidation competency of palladium nanocatalysts over ceria-carbon composite supports during alkaline ethylene glycol oxidation, *Catal. Sci. Technol.*, 2019, **9**(2), 493–501, DOI: **10.1039/c8cy02232a**.

45 S. S. Medany, M. A. Hefnawy and S. M. Kamal, High-performance spinel NiMn2O4 supported carbon felt for effective electrochemical conversion of ethylene glycol and hydrogen evolution applications, *Sci. Rep.*, 2024, **14**(1), 1–13, DOI: **10.1038/s41598-023-50950-3**.

46 Z. Wang, *et al.*, Coproduction of Glycolic Acid and Hydrogen by Electroreforming Ethylene Glycol Using Palladium-Copper Hydride Hyperbranched Nanocrystals, *ACS Appl. Nano Mater.*, 2024, **7**(13), 15841–15847, DOI: **10.1021/acsanm.4c03232**.

47 Y. Chen, *et al.*, Trimetallic PtRhCo petal-assembled alloyed nanoflowers as efficient and stable bifunctional electrocatalyst for ethylene glycol oxidation and hydrogen evolution reactions, *J. Colloid Interface Sci.*, 2020, **559**, 206–214, DOI: **10.1016/j.jcis.2019.10.024**.

48 M. S. Amer, *et al.*, Gray mesoporous SnO2 catalyst for CO2 electroreduction with high partial current density and formate selectivity, *Environ. Res.*, 2024, **252**, 118897, DOI: **10.1016/j.envres.2024.118897**.

49 M. S. Amer, H. A. AlOraij and A. M. Al-Mayouf, Facial synthesis of high-performance Ni doped-tin oxide mesoporous for CO2 electroreduction to formate, *J. CO2 Util.*, 2024, **82**, 102742, DOI: **10.1016/j.jcou.2024.102742**.